The Effect of Carbide Concentration at Grain Boundaries on Thermal Stresses in Castings for Heat Treatment Furnace Tooling

A. Bajwoluk * iD **, P. Gutowski** iD

Mechanical Engineering Faculty, West Pomeranian University of Technology, Szczecin
Al. Piastów 19, 70-310 Szczecin, Poland
* Corresponding author: E-mail address: Artur.Bajwoluk@zut.edu.pl

Abstract

Austenitic Fe-Ni-Cr alloys are commonly used for the production of castings intended for high-temperature applications. One area where Fe-Ni-Cr castings are widely used is the equipment for heat treatment furnaces. Despite the good heat resistance properties of the materials used for the castings, they tend to develop cracks and deformations over time due to cyclic temperature changes experienced under high temperature operating conditions. In the case of carburizing furnace equipment, thermal stresses induced by the temperature gradient in each operating cycle on rapidly cooled elements have a significant influence on the progressive fatigue changes. In the carburized subsurface zone, also the different thermal expansion of the matrix and non-metallic precipitates plays a significant role in stress distribution. This article presents the results of analyses of thermal stresses in the surface and subsurface layer of carburized alloy during cooling, taking into account the simultaneous effect of both mentioned stress sources. The basis for the stress analyzes were the temperature distribution in the cross-section of the cooled element as a function cooling time, determined numerically using FEM. These distributions were taken as the thermal load of the element. The study presents the results of analyses on the influence of carbide concentration increase on stress distribution changes caused by the temperature gradient. The simultaneous consideration of both thermal stress sources, i.e. temperature gradient and different thermal expansions of phases, allowed for obtaining qualitatively closer results than analyzing the stress sources independently.

Keywords: Cast grates, Thermal stresses, Heat treatment equipment, Thermal shock

1. Introduction

Castings made of austenitic alloys with high nickel and chromium content find broad application in industrial sectors where materials are required to withstand high temperature, thermal shocks, and exhibit good creep resistance [1-7]. An example of such an area is the use of these castings in furnaces for heat treatment. Due to their excellent heat resistance, castings made of Fe-Ni-Cr are utilized in these applications, serving, among other uses, as equipment for transporting heat-treated loads [1-3, 6, 8-9].

The cyclic operation under elevated and high temperature and its rapid changes promotes the progression of fatigue processes, resulting in the initiation and growth of cracks that disqualify castings from further use [10-15]. The formation of these cracks is significantly influenced by thermal stresses generated in the

castings in each successive cycle of operation during each temperature change.

In rapidly cooled castings used in furnaces for heat treatment, the main source of thermal stresses is the temperature gradient caused by the variable and uneven distribution of temperature over time. In the case of equipment for carburizing furnaces, due to the formation of a carburized layer in the subsurface zone of the castings, an additional source of thermal stresses is the different thermal expansion of non-metallic precipitates and the austenitic matrix [3, 16].

In the work [17], the authors emphasized that in rapidly cooled components, actual stresses caused by the different thermal expansion between non-metallic precipitates and the metallic matrix can be significantly higher than stresses determined with a simplified approach treating the carburized casting as a composite consisting of a carburized subsurface zone and a non-carburized core. The possibility of high stresses occurring in non-metallic precipitates and their surroundings during rapid cooling processes is confirmed by the results of analyses presented in previous studies [16, 18, 19]. However, these studies overlooked the influence of the temperature gradient that occurs during cooling, assuming the temperature change as a simultaneous process throughout the entire material volume.

On the other hand, in the publications [20-24], comprehensive analyses are presented on the stresses arising in the structures of technological equipment for furnaces, including stresses induced by temperature gradients. The studies also explore the possibilities of reducing these stresses through various geometrical modifications of the equipment. In the referenced works, the only source of thermal stresses taken into account was the temperature gradient.

In real castings used in carburizing furnaces, both of the aforementioned sources of stresses act simultaneously. However, in previous analyses, this fact was not taken into account. It was only in the article [25] that comparative analyses of thermal stresses in the carburized alloy's subsurface layer were presented, considering both of these sources independently and accounting for their simultaneous interaction. The stress distributions obtained for the latter case best explained the cracks formation observed in actual castings.

This paper presents the results of numerical analyses of the impact of increasing carbide precipitate concentration at grain boundaries on the distribution of thermal stresses in the subsurface layer of castings of technological equipment for carburizing furnaces during rapid cooling.

It has been demonstrated that with a high concentration of carbide precipitates at grain boundaries and an appropriate depth of the carburized layer, tensile stresses can develop on the surface of the component at the grain boundary. Such stresses promote the initiation and propagation of cracks along this boundary from the surface into the material.

2. Object of study

During heat treatment processes, components such as shafts, gears, etc., undergo this treatment in furnaces on specially designed technological equipment. A significant part of such equipment, including trays and baskets, is produced in the form of thin-walled openwork castings (Fig. 1) [3, 8, 16, 20-24]. Due to the operating conditions on heat treatment lines, i.e., high temperature and its rapid changes, as well as mechanical loading from the load, these castings are made from heat-resistant austenitic Fe-Ni-Cr alloys.
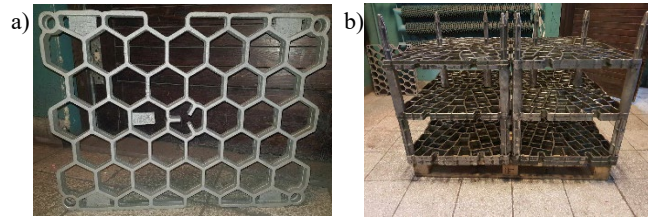

Fig. 1. Equipment for transporting loads in heat treatment furnaces: a) pallet, b) three-level assembly

Despite the high heat resistance of these alloys, cyclic operation in furnaces over time leads to fatigue-related changes in the equipment elements, resulting in the initiation and growth of cracks. These cracks most commonly occur at grain boundaries, especially in areas with a high concentration of carbides (Fig. 2). Due to the progressive fatigue processes occurring in successive cycles of operation, these cracks propagate into the material, which can lead to the complete discontinuity of the casting walls and the need to withdraw these castings from further use [3, 17].
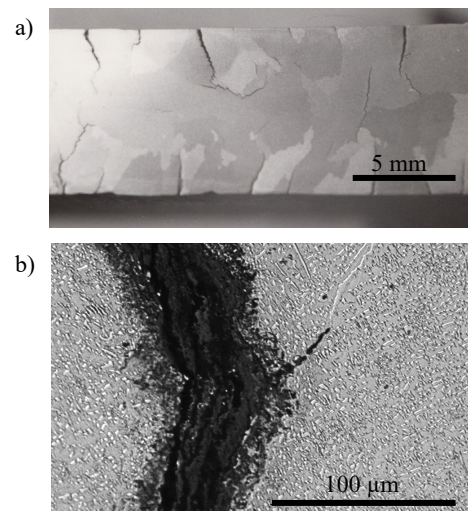

Fig. 2. Cracks on the wall of a tray for carburizing furnaces made of 1.4849 cast steel: a) crack on the tray rib, b) optical microscope image of crack in carburized subsurface zone

3. FEM model of carburized layer

Numerical analyses of thermal stress distribution in castings of heat treatment equipment, taking into account the simultaneous influence of temperature gradient and different thermal expansion of phases, were conducted on a Finite Element Method (FEM) model of a slice of the pallet rib. The modeled slice (Fig. 3) covered the area of the subsurface zone of the pallet rib, including the oxide layer formed on the casting surface, the carburized layer developing into the material, and the non-carburized core.

According to the notations on Fig. 3, the model had dimensions: $a = 4$ mm, $b = 4$ mm, $h = 6$ mm.

In the model, it was assumed that carbide precipitates are located at the grain boundaries of the austenite, neglecting the presence of carbides inside the grains themselves. Furthermore, for the sake of simplification, the actual network of carbide precipitates with any shape (Fig. 3a) was replaced by an ordered set of their rectangular precipitates (Fig. 3b) located in one yz plane, which simultaneously constituted the adopted grain boundary.
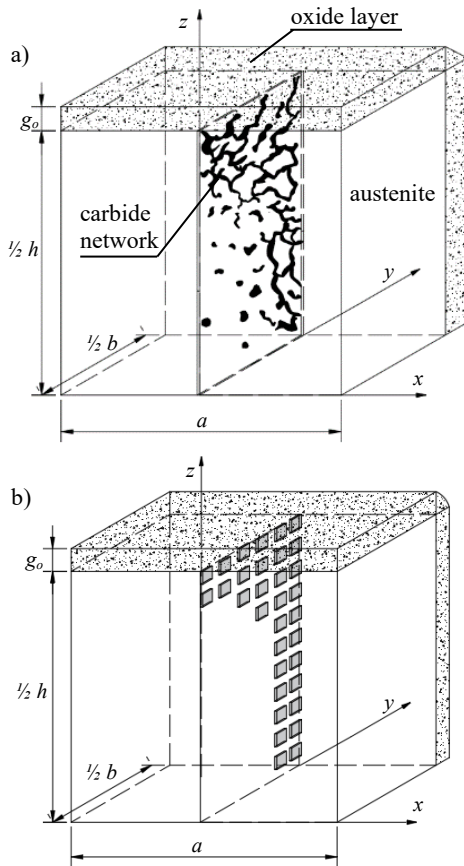

Fig. 3. The modelled carburized layer in furnace equipment:
a) carbide network model at the grain boundary, b) simplified model with cuboidal regions of carbide precipitation

It was assumed that the oxide layer covering the alloy has a thickness equal to $g_o = 5$ μm. This layer exhibits different thermal expansion compared to austenite. Therefore, its presence has a significant impact on the distribution of thermal stresses generated in the subsurface zone of the castings during temperature change processes.

To analyze the influence of the growth of the carburized layer on the resulting stress distributions, in successive calculation steps, the growth of this layer was simulated. This was achieved by increasing the dimensions of existing carbide precipitate areas (simultaneously decreasing the distance between them) and simulating the formation and development of new precipitates at a greater distance from the surface. The four stages of carbide network growth adopted in the calculations are presented in Fig 4. To reduce the number of finite elements used and thus optimize computation time, we limited the occurrence of carbide precipitate areas to the corner region of the rib ($y = z = 200$ μm), where the highest temperature gradient occurs during cooling.
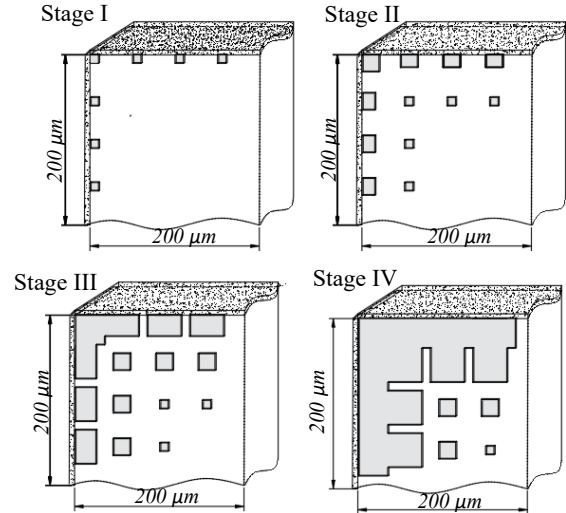

Fig. 4. Stages of carbide network growth adopted in the analyses

The dimensions of cuboidal carbide precipitates for each of the analyzed stages can be expressed using the appropriate dimension matrix adopted in the analyses as follows:

$$\text{stage I} - \begin{bmatrix} 10 & 10 & 10 & 10 \\ 10 & 0 & 0 & 0 \\ 10 & 0 & 0 & 0 \\ 10 & 0 & 0 & 0 \end{bmatrix}; \quad \text{stage II} - \begin{bmatrix} 20 & 20 & 20 & 20 \\ 15 & 10 & 10 & 10 \\ 15 & 10 & 0 & 0 \\ 15 & 10 & 0 & 0 \end{bmatrix}$$

$$\text{stage III} - \begin{bmatrix} 35 & 40 & 40 & 40 \\ 25 & 20 & 20 & 20 \\ 25 & 20 & 10 & 10 \\ 25 & 20 & 10 & 0 \end{bmatrix}; \quad \text{stage IV} - \begin{bmatrix} 35 & 60 & 60 & 60 \\ 35 & 40 & 40 & 40 \\ 35 & 40 & 20 & 20 \\ 35 & 40 & 20 & 10 \end{bmatrix}$$

The dimensions along the y-axis and the z-axis of individual carbide precipitate areas can be read from these matrices using the formula:

$$y_{ij} = a_{ij}^k [\mu m]$$
$$z_{ij} = a_{ji}^k [\mu m]$$

where y_{ij} and z_{ij} are the dimensions along the y-axis and z-axis of area ij, and a_{ij}^k represents the element ij of the matrix for stage k. The dimension along the x-axis for all carbide areas was assumed to be equal to 8 μm.

In the case of stage 3 and 4, it is evident that carbide precipitate areas in the most carburized zones overlap due to the assumed growth. In such a case, it was assumed that these areas merge and in the analyses, they constitute a single shared precipitate area.

Both FEM models (Fig. 5a, b) and calculations conducted as part of the article were carried out using the MIDAS NFX 2017 software. In the analyses, a finite element mesh consisting of 8-nodes, linear, isoparametric hexahedron elements was applied (Fig.

5c) with various dimensions. The following shape function was adopted for these elements [26, 27]:

$$N_i = \frac{1}{8}(1 + \xi_i\xi)(1 + \eta_i\eta)(1 + \zeta_i\zeta) \qquad (1)$$
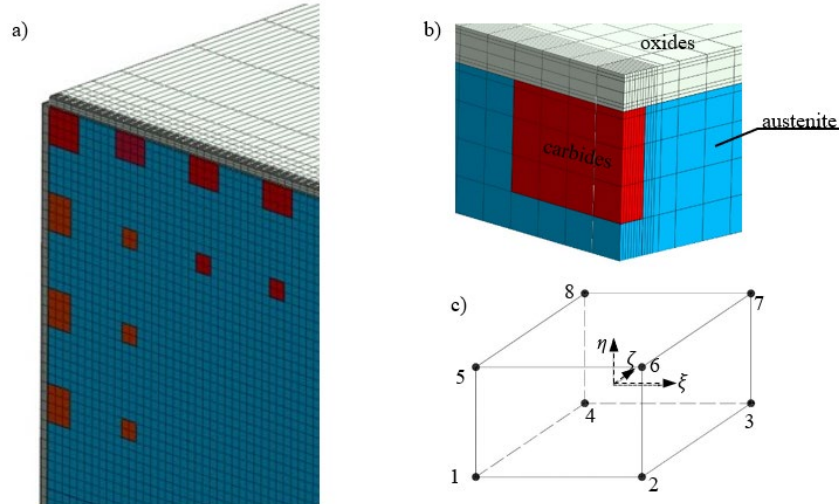
Rys. 5. Adopted FEM mesh: a) example of mesh for stage 2 of the carbide network growth, b) finite elements in the vicinity of carbide c) node locations of a hexahedron element and natural coordinate system

4. Adopted methodology

The uneven volumetric changes occurring in the casting during each temperature change are the cause of the analyzed thermal stresses. Therefore, the first step in the conducted analyses was to perform numerical calculations of temperature distribution changes in the subsurface layer of the casting during the cooling process. In these analyses, it was assumed that heat exchange with the environment occurs through free convection, while heat flow within the model occurs through conduction. The heat transfer module of the Midas NFX 2017 software, designed for transient heat flow simulation analyses, was used for the calculations. In this module, the energy balance equation is utilized as the basis for the calculations:

$$\Delta E = \Delta E_T + \Delta E_G \qquad (2)$$

where:
ΔE – change of internal energy of the analyzed object,
ΔE_T – heat flux transferred across the object's boundaries,
ΔE_G – internal heat generated by the object.

The above equation can be written in the following form:

$$\int_\Omega c\rho\dot{T}d\Omega = \int_{S_h} qdS + \int_\Omega rd\Omega \qquad (3)$$

where:
c – specific heat of the material from which the object is made,
ρ – mass density,
$\dot{T}$ – ratio of temperature T change in time t,

Ω – element volume,
q – density of the heat flux passing through the boundary surface of the object,
S – object boundary surface,
S_h – boundary surface through which heat flows,
r – quantity of heat generated per unit volume.

After substituting Fourier's law:

$$q = -\lambda(T)\nabla T \qquad (4)$$

where:
$\lambda(T)$ – function that determines the dependence of thermal conductivity of material on the temperature,
∇T – temperature gradient,
and if variation δT is taken, the following equation is attained:

$$\int_\Omega c\rho\dot{T}\delta Td\Omega + \int_\Omega \frac{\partial\delta T}{\partial x_i}\lambda_{ij}(T)\frac{\partial T}{\partial x_j}d\Omega = \\ = \int_{S_{hq}} q_{ext}\delta TdS + \int_\Omega r\delta Td\Omega \qquad (5)$$

Since in the numerical calculation software Midas NFX 2017 utilized in the analysis the temperature is interpolated as a shape function of the form of:

$$T = N_i(x)T_i \qquad (6)$$

the equation (5) becomes the following nonlinear simultaneous equation consisted of nodal temperature, which includes a temperature differential term with respect to time:

$$C(T_i)\dot{T} + \lambda(T_i)T = R(q_{ext}, r) \qquad (7)$$

where:
$C(T_i)$– matrix of heat capacity,
$\lambda(T_i)$– matrix of thermal conductivity,
$R(q_{ext}, r)$– matrix of thermal load.

In the applied module for determining the history of temperature distribution changes, the backward difference method is used. The equation (7) in the consecutive time step can be described as follows:

$$\left[\frac{C(T_i(t+\Delta t))}{\Delta t} + \lambda(T_i(t+\Delta t))\right]T(t+\Delta t) + $$
$$-\frac{C(T_i(t+\Delta t))}{\Delta t}T(t) - R(q_{ext}, r) = 0 \qquad (8)$$

Temperature distributions in successive cooling process steps are determined by applying the above equation again, using the Newton-Raphson method.[26, 27]

In the heat flow analyses, for the sake of simplification, uniform thermal properties of the material were assumed at each point in the model. Based on the data in the standard [28] for the commonly used carburizing furnace steel 1.4849 (GX40NiCrSiNb38-19), the following properties were adopted: specific heat $c = 500$ J/(kg·K) and a temperature-dependent thermal conductivity coefficient λ, in accordance with the data provided in Table 1. The density of the material was adopted as $\rho = 7800$ kg/m³.

Table 1.
The coefficient of thermal conduction λ of cast steel 1.4849 [28]

Temperature T, °C	20	100	800	1000
Coefficient λ, W/(m·K)	12	12.3	23.3	26.5

In the analyses, it was assumed that the initial temperature was 900 °C, and the cooling medium was quenching oil at a temperature $T_k = 20$ °C. In the study, an empirically determined [22] heat transfer coefficient curve was adopted, as shown in the chart in Fig. 6. The calculations were performed for the first four seconds of the cooling process, with a computational step of 0.02 seconds.
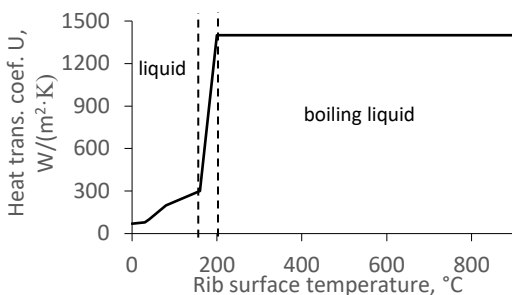

Fig. 6. The adopted relationship between the heat transfer coefficient and temperature in the analyses [22]

The next stage of the conducted research was to take the obtained results of temperature distribution changes as input data for thermal stress analysis. In these analyses, a rapid change in temperature was assumed as the load, starting from the initial temperature, which was $T_0 = 900$ °C at each node of the model, to the temperature obtained for these nodes at successive times t_i during the cooling process. This procedure was performed for all adopted stages of carbide network growth.

In the stress analyses, degrees of freedom were constrained for nodes lying on the central planes of the model, i.e., on the xy, yz, and zx planes, in directions perpendicular to these planes. The remaining nodes were unconstrained. The applied method of constraining the nodes of the model is shown in Fig. 7.
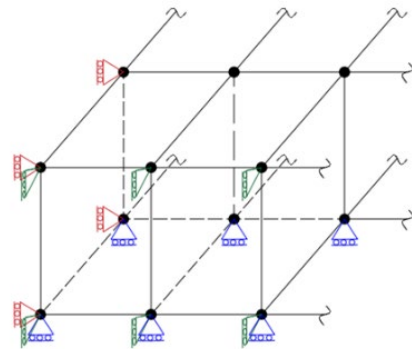
Rys. 7. Constrains of nodes adopted in the FEM model

In the calculations, an elastic model of material was used for carbides and oxides, while studies of the austenite were based on an elastic-plastic model with nonlinear hardening, in which the true tensile curve was approximated with several line segments characterized by different values of the hardening modulus E_{ai}. The stress-strain curve adopted for austenite in numerical calculations is shown in Fig. 8. The parameters assumed in the stress calculations for austenite [16, 28, 29], carbides [8, 16] and oxides [30-38] are presented in table 2. It is worth to note that technical literature provides a wide range of Young's modulus values for chromium oxides, depending on the conditions of the formation of an oxide layer, its density, and the adopted measurement method. Therefore, in the present calculations, the average value determined from the data contained in publications [32-38] was adopted.

Table 2.
Materials parameters adopted in thermal stress analysis

Parameter	austenite	M_7C_3	Cr_2O_3
Young modulus E, GPa	173	294	214
Yield strength R_e, MPa	208	-	-
Strain hardening modulus E_1, GPa	4.09	-	-
Poisson ratio v	0.253	0.372	0.270
Thermal expansion coefficient α, 1/K	17.7 · 10⁻⁶	8.6 · 10⁻⁶	7.5 · 10⁻⁶

Due to the strong orientation of the models adopted in the calculations, resulting from the distribution of carbide areas along

the grain boundary, directional stresses σ_x, i.e., normal stresses perpendicular to the yz plane in which this boundary is located, were adopted as the main criterion for stress assessment.
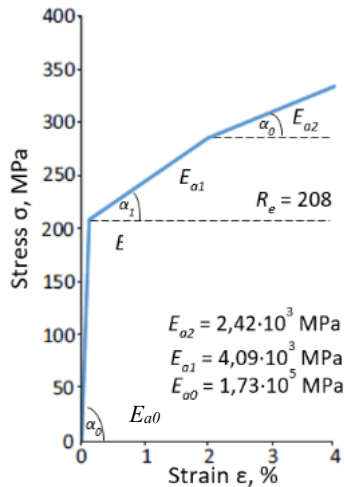

Fig. 8. Austenite stress-strain diagram adopted in analyzes [16]

5. Results and discussion

As a result of the conducted numerical heat flow analyses, temperature distributions in successive moments of the cooling process were determined in the analyzed model. An exemplary temperature distribution determined for the time $t_i = 0.5$ second is presented in Fig. 9.
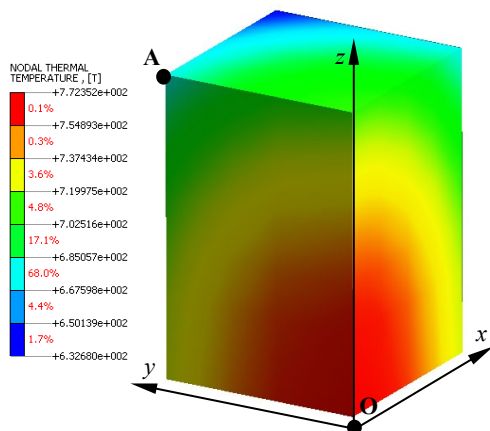

Fig. 9. Temperature distribution in the analyzed model after $t_i = 0.5$ s of the cooling time

In Fig. 10, the temperature changes at the edge of the surface (point A) and in the center (point O) of the assumed rib cross-section (according to the markings in Fig. 9) are presented. Meanwhile, Fig. 11 illustrates the temperature difference between these points over the cooling time. It can be observed that even with a relatively small thickness of the modeled rib ($b = 4$ mm), the temperature differences between the surface and the core of the model are significant. The maximum temperature difference in the O-A direction occurred after the cooling time $t_{max} = 0.42$ seconds
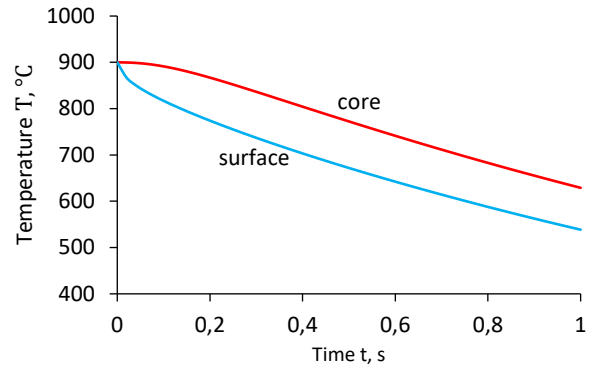
and was equal to $\Delta T_{max} = 101$ °C.

Fig. 10. Change in temperature distribution at the surface (point A) and in the core (point O) of the model
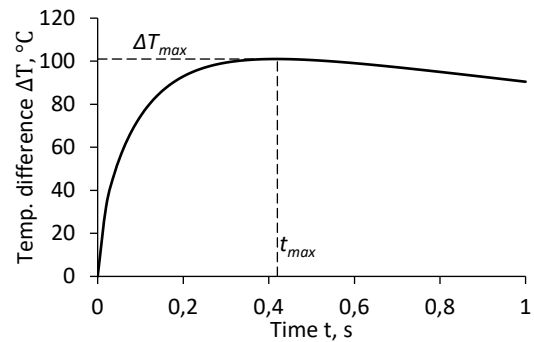

Fig. 11. Change in temperature difference between points A and O

The results of thermal stress analyses determined for the change in temperature from the initial T_0 to the distribution determined after time t_{max} are presented in Fig. 12-14.
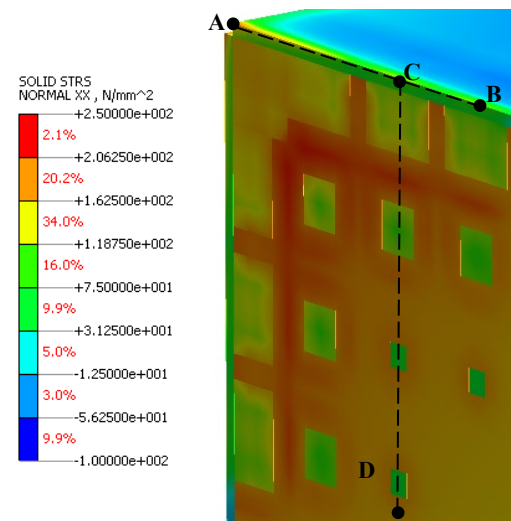

Fig. 12. Distribution of stresses σ_x obtained for the third stage of the assumed carbide network growth

In Fig. 12, an exemplary distribution of σ_x stresses is presented, obtained for the third of the assumed stages of carbide network growth. It can be seen that the presence of carbides influenced both the change in stress distribution in the surface layer of oxides and the stresses in the lower carburized zone. Two directions, A-B and C-D, were also marked on Fig. 12, along which the results of stress distributions in successive stages of carbide network growth (Fig. 4) were analyzed. The A-B direction illustrates the stress distribution in the surface oxide layer, located above the carbide precipitate areas, while the C-D direction shows the stress distribution from the surface into the material.

The σ_x stress distributions σ_x along the A-B direction are shown in Fig. 13. In this figure, in addition to the results obtained for each of the four assumed stages of carburized layer growth, a reference stress distribution determined in the absence of carbide precipitates is also included for comparison, marked with the symbol 0.

In the reference case, as expected, compressive stresses are generated in the surface layer of oxides due to cooling. Analyzing the presented results, it can be observed that the appearance and growth of carbide precipitate areas in successive stages of carburizing significantly influenced the distribution of local thermal stresses. Already in the first of the assumed stages of carburized layer growth, the presence of relatively small individual carbide precipitates caused a significant reduction in compressive stresses in the layer of oxides above them, and tensile stresses appeared at the corner (point A). In the second of the assumed stages, tensile stresses at the corner increased significantly, and additionally, in the layer of oxides above the areas of carbide precipitates below, local tensile stresses appeared. With further densification of carbide precipitate areas, σ_x stresses in the layer of oxides increased. In stage III, the stresses in the oxide layer above the carbide precipitates along the entire precipitate line took positive values – they were tensile, reaching values above 200 MPa

in the model for stage IV.
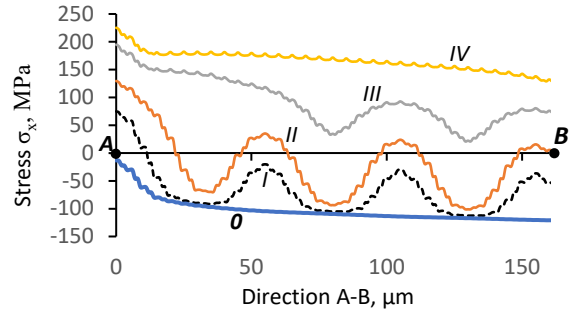
Rys. 13. Stress σ_x distributions along the line A-B

In Fig. 14, σ_x stress distributions along the C-D direction in successive stages of carbide precipitate growth are presented. Based on the presented charts, it can be stated that the obtained stress distributions are predominantly influenced by stresses caused by the temperature gradient. However, the presence of carbide precipitate areas significantly affected local changes in the obtained stress distributions, with σ_x stresses in the carbide precipitate areas being tensile in all four analyzed carburizing stages.

As also evident in Fig. 13, with the growth of carbide precipitate areas in the subsurface zone of the model, stresses in the oxide layer change their character from compressive to tensile not only on the surface of this layer but throughout its thickness. This promotes, under conditions of cyclic temperature changes in successive cycles of operation, the formation of cracks and the interruption of the continuity of the oxide layer.
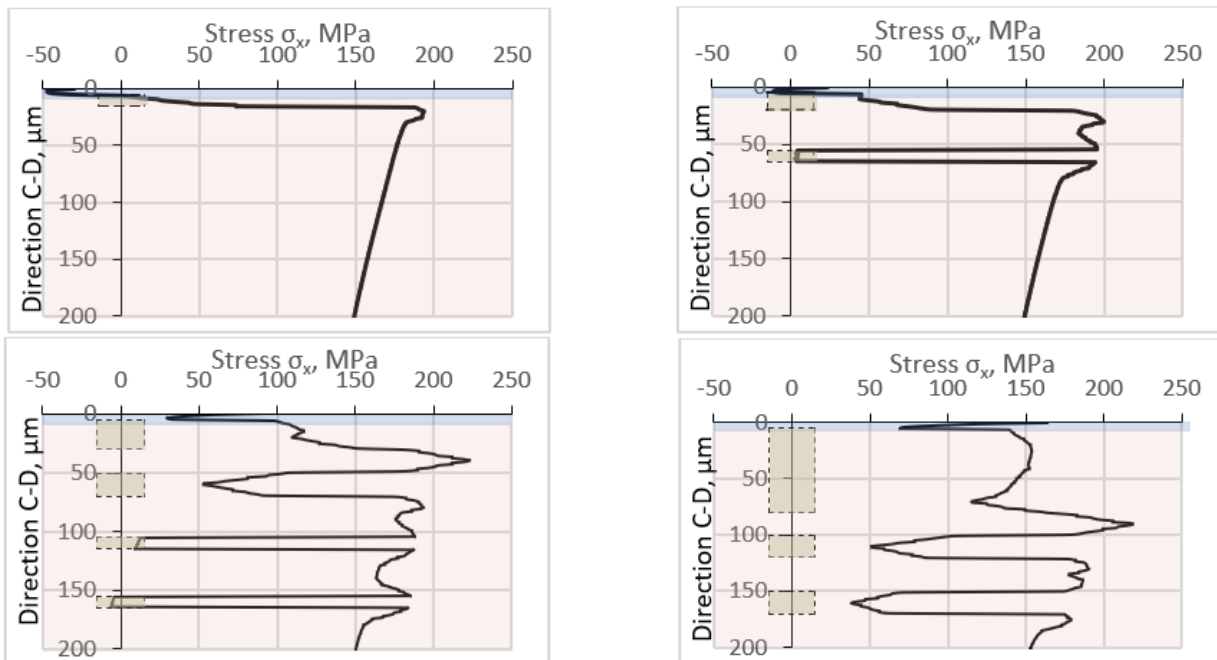

Fig. 14. Stress σ_x distribution along the line CD: a) stage I, b) stage II, c) stage III, d) stage IV

In numerical analyses considering only stresses caused by the different thermal expansion of carbides and the surrounding matrix [16, 18, 19], compressive stresses were observed in the carbides surrounded on all sides by the austenitic matrix. From the presented graphs, it is evident that when both the stresses induced by the temperature gradient and the different thermal expansion of phases are considered simultaneously, the stress distribution may change. Under the simultaneous influence of the examined stress sources, tensile stresses were also present in carbide areas located further from the surface, fully surrounded by the austenitic matrix. Although these tensile stresses are lower than those in the surrounding austenitic matrix, they generally do not change sign despite the local decrease in value. Furthermore, it can be observed that the tensile stresses in carbides increase with the expansion of carbide areas.

The development of tensile stresses in the oxide layer during rapid cooling processes can lead to the initiation of cracks in this layer. This phenomenon promotes the progression of the carburization process in the alloy, and thus further changes in the functional properties of the casting material.

d) The presence of tensile stresses in both surface oxide layer and deeper carburized layer promotes the propagation of cracks along grain boundaries, especially in regions with increased concentration of carbides, particularly at the carbide-austenite boundary.

6. Summary

At work, a numerical analysis of thermal stress development was conducted, taking into account the simultaneous impact of two main sources of these stresses: temperature gradient and thermal mismatch of structural components. In the conducted analyses, the influence of increasing concentration of carbide precipitation areas on the local changes in stresses caused by the temperature gradient during the rapid cooling process of heat treatment equipment components was examined.

Despite the predominant nature of stresses caused by the temperature gradient, the presence of carbides significantly influenced the local stress distribution. Already in the second of the adopted stages of carbide network growth, their presence led to the formation of tensile stresses in the surface layer of oxides, which can lead to the formation of cracks in this layer. Due to the influence of the temperature gradient, tensile stresses also form in the carbides surrounded on all sides by austenite during cooling what can lead to the progress of cracks deep into the material.

Based on the obtained results, it can be concluded that the increasing concentration of carbide precipitation areas is a factor contributing to the development of tensile stresses during rapid cooling, both in the surface oxide layer and in the carbides themselves, including those fully surrounded by the austenitic matrix.

The obtained results better explain the formation of actual cracks than the results obtained when considering both sources of stress independently.

References

[1] Lai, G.Y. (2007). *High-Temperature Corrosion and Materials Applications*. ASM International.

[2] Davis, J.R. (1997). Industrial applications of heat-resistant materials. *In Heat Resistant Materials.* 67-85.

[3] Piekarski, B. (2012). *Creep-resistant castings used in heat treatment furnaces.* Szczecin: West Pomeranian University of Technology Publishing House. (in Polish).

[4] Lo, K.H., Shek, C. H. & Lai, J.K.L. (2009). Recent developments in stainless steels. *Materials Science and Engineering R: Reports.* 65(4-6), 39-104.

[5] Carreon, M., Ramos Azpeitia, M.O., Hernandez Rivera, J.L., Bedolla Jacuinde, A., Garcia Lopez, C. J., Ruiz Ochoa, J.A. & Gonzalez Castillo, A.C. (2023). Development of a novel heat-resistant austenitic cast steel with an improved thermal fatigue resistance. *International Journal of Metalcasting.* 17(2), 1114-1127. DOI: 10.1007/s40962-022-00838-1.

[6] Drotlew, A., Garbiak, M. & Piekarski, B. (2012). Cast steels for creep-resistant parts used in heat-treatment plants. *Archives of Foundry Engineering*, 12(4), 31-38. DOI: 10.2478/v10266-012-0103-0.

[7] Lekakh, S.N., Buchely, M., Li, M. & Godlewski, L. (2023). Effect of Cr and Ni concentrations on resilience of cast Nb-alloyed heat resistant austenitic steels at extreme high temperatures. *Materials Science and Engineering: A.* 873, 145027. DOI: doi.org/10.1016/j.msea.2023.145027.

[8] Piekarski, B. & Drotlew, A. (2019). Cast grates used in heat treatment furnaces. *Archives of Foundry Engineering*, 19(3), 49-54. DOI: 10.24425/afe.2019.127138.

[9] Nandwana, D., Bhupendra, N.K., Bhargava, T., Nandwana, K. & Jawale, G. (2010). Design, Finite Element analysis and optimization of HRC trays used in heat treatment process. *Proceedings of the World Congress on Engineering WCE* 2010, (II), (pp. 1149-1154).

[10] Ul-Hamid, A., Tawancy, H.M., Mohammed, A.R.I. & Abbas, N.M. (2006). Failure analysis of furnace tubes exposed to excessive temperature. *Engineering Failure Analysis.* 13(6), 1005-1021. DOI: 10.1016/j.engfailanal. 2005.04.003.

[11] Piekarski, B. (2010). Damage of heat-resistant castings in a carburizing furnace. *Engineering Failure Analysis.* 17(1), 143-149. DOI: 10.1016/j.engfailanal.2009.04.011.

[12] Reihani, A., Razavi, S.A., Abbasi, E. & Etemadi, A.R. (2013). Failure analysis of welded radiant tubes made of cast heat-resisting steel. *Journal of failure Analysis and Prevention.* 13(6), 658-665. DOI: 10.1007/s11668-013-9741-y.

[13] Bochnakowski, W., Szyller, Ł. & Osetek, M. (2019). Damage characterization of belt conveyor made of the 330Nb alloy after service in a carburizing atmosphere in a continuous heat treatment furnace. *Engineering Failure Analysis.* 103, 173-183. DOI: 10.1016/j.engfailanal.2019.04.058.

[14] González-Ciordia, B., Fernández, B., Artola, G., Muro, M., Sanz, Á. & López de Lacalle, L.N. (2019). Failure-analysis based redesign of furnace conveyor system components: a case study. *Metals.* 9(8), 816, 1-12. DOI: 10.3390/met9080816.

[15] Srikanth, S., Saravanan, P., Khalkho, B. & Banerjee, P. (2021). Failure analysis of inconel 601 radiant tubes in continuous annealing furnace of hot dip galvanizing line. *Journal of*

Failure Analysis and Preven-tion, 21. 747-758. DOI: 10.1007/s11668-021-01148-0.

[16] Gutowski, P. (1989). *Analysis of cracking causes in grates used in carburising furnaces*. Szczecin: Diss., Politechnika Szczecińska. (in Polish).

[17] Schnaas, A. & Grabke, H.J. (1978). High-Temperature Corrosion and Creep of Ni-Cr-Fe Alloys in Carburizing and Oxidizing Environments. *Oxidation of Metals.* 12(5), 387-404. https://doi.org/10.1007/BF00612086.

[18] Zatorski, Z. & Tuleja, J. (2017). Numerical modelling of micro-stresses in carbonised austenitic cast steel under rapid cooling conditions. *Archives of Metallurgy and Materials.* 62(2), 635-641. DOI: 10.1515/amm-2017-0093.

[19] Bajwoluk, A. & Gutowski, P. (2019). Stress and crack propagation in the surface layer of carburized stable austenitic alloys during cooling. *Materials at High Temperatures.* 36(1), 9-18. DOI: 10.1080/09603409.2018144 8528.

[20] Bajwoluk, A. & Gutowski, P. (2017). The effect of cooling agent on stress and deformation of charge-loaded cast pallets. *Archives of Foundry Engineering.* 17(4), 13-18. DOI: 10.1515/afe-2017-0123.

[21] Bajwoluk, A. & Gutowski, P. (2018). Design options to decrease the thermal stresses in cast accessories for heat and chemical treatment furnaces. *Archives of Foundry Engineering.* 18(4), 125-130. DOI:10.24425/afe.2018. 125181.

[22] Bajwoluk, A. & Gutowski, P. (2019). Thermal stresses in the accessories of heat treatment furnaces vs cooling kinetics. *Archives of Foundry Engineering.* 19(3), 88-93. DOI: 10.24425/afe.2019.127146.

[23] Bajwoluk, A. & Gutowski, P. (2021). Effect of thermal nodes reduction in wall connections of the charge-handling furnace grates on thermal stresses. *Archives of Foundry Engineering.* 21(3), 53-58. DOI: 10.24425/afe.2021.138665.

[24] Tuleja, J., Kędzierska, K. & Sowa, M. (2022). The use of the finite element method to locate the places of damage occurrence in elements of technological equipment in carburizing furnaces. *Procedia Computer Science.* 207, 3931-3937. DOI: 10.1016/j.procs.2022.09.455.

[25] Bajwoluk, A. & Gutowski, P. (2023). Analysis of thermal stresses synergy in surface layer of carburised creep-resistant casts during rapid cooling processes. *Materials at High Temperatures.* 40(1), 64-76. DOI: 10.1080/09603409.2022. 2162684.

[26] Zienkiewicz, O.C. (1971). *Finite element method in engineering science*. London: McGraw-Hill.

[27] Midas NFX 2017: Analysis Manual, 2017.

[28] Standard PN-EN 10295: 2004. Heat resistant steel castings.

[29] Church, B.C., Sanders, T.H., Speyer, R.F. & Cochran, J.K. (2007). Thermal expansion matching and oxidation resistance of Fe–Ni–Cr interconnect alloys. *Material Science and Engineering A.* 452-453. https://doi.org/10.1016/j.msea.2006.10.149.

[30] Guo, X., Liu, Z., Li, L., Cheng, J., Su, H. & Zhang, L. (2022). Revealing the long-term oxidation and carburization mechanism of 310S SS and Alloy 800H exposed to supercritical carbon dioxide. *Materials Chararacterization.* 183, 111603. DOI: 10.1016/j.matchar.2021.111603.

[31] Shaffer, P.T.B. (1964). Plenum Press Handbooks Of High-Temperature Materials, Springer Science + Business Media.

[32] Schutze, M. (1997). *Protective oxide scales and their breakdown*. Ed. by D. R. Holmes, Institute of Corrosion, John Wiley & Sons.

[33] Huntz, A.M. (1995). Stresses in NiO, Cr_2O_3, and A_2O_3, oxide, *Mater Science and Engineering A.* 201 (1-2), 211-228. https://doi.org/10.1007/BF02648633.

[34] Richard, C.S., Béranger, G. & Decomps, F. (1995). Study of Cr_2O_3 coatings Part I: Microstructures and modulus. *Journal of Thermal Spray Technology.* 4(4), 342-346. https://doi.org/10.1007/BF02648633.

[35] Pang, X., Gao, K. & Volinsky, A.A. (2007). Microstructure and mechanical properties of chromium oxide coatings. *Journal of Materials Research.* 22(12), 3531-3537.

[36] Ji, A.L., Wang, W., Song, G.H., Wang, Q.M., Sun, C. & Wen, L.S. (2004). Microstructures and mechanical properties of chromium oxide films by arc ion plating. *Materials Letters.* 58(14), 1993-1998. https://doi.org/10.1016/j.matlet. 2003.12.029.

[37] Barshilia, H.C. & Rajam, K.S. (2008). Growth and characterization of chromium oxide coatings prepared by pulsed-direct current reactive unbalanced magnetron sputtering. *Applied Surface Science.* 255(9), 2925-2931. https://doi.org/10.1016/j.apsusc.2008.08.057.

[38] Gaillac, R., Pullumbi, P. & Coudert, F.X. (2016). ELATE: an open-source online application for analysis and visualization of elastic tensors. *Journal of Physics: Condensed Matter.* 28(27), 275201.